International Journal of Heat and Mass Transfer 52 (2009) 1481–1487

Contents lists available at ScienceDirect

International Journal of Heat and Mass Transfer

journal homepage: www.elsevier.com/locate/ijhmt

Drag force acting on bubbles in a subchannel of triangular array of rods

Gabor Hazi *, Gusztav Mayer, Attila Markus

MTA KFKI Atomic Energy Research Institute, Theoretical Thermohydraulics Research Group, H-1525 Budapest, Hungary

ARTICLE INFO

Article history:
Received 27 May 2008
Available online 14 October 2008

ABSTRACT

Forces acting on spherical bubbles in a subchannel of a rod bundle with triangular rod arrangement (the pitch to diameter ratio is $P/D = 1.34$) have been studied at low bubble Reynolds numbers $O(0.1) - O(1)$. The bubble motion has been simulated resolving the interface of the bubble by using the lattice Boltzmann method. Steady drag and virtual mass forces have been determined from the simulation results. Based on the simulation data, the relation $C_D = 16.375/Re_T$ could be established between the steady drag coefficient C_D and the terminal Reynolds number Re_T when the diameter ratio $\lambda = d/D$ of the bubble d and the channel D is less than 0.2. It is found that the virtual mass coefficient can achieve as high value as 7.2, which is a consequence of strong wall effects. Considering interactions between bubbles, cooperation in the axial direction and hindering in the lateral direction could be observed. We demonstrate that the relation between the terminal velocity of a bubble and that of the suspension follows a Richardson–Zaki like correlation, but the exponent is not only a function of the Eotvos and Morton numbers, but it also depends on the particle configuration.

1. Introduction

For accurate large scale modeling of industrial two-phase flow problems we need reliable models for interfacial mass, momentum and energy transfers. In case of bubble flows, the interfacial momentum transfer is due to the forces acting between the liquid phase and the gas bubbles. The problem of evaluating the hydrodynamic forces acting on a bubble in a fluid is a long standing problem. Models used for predicting forces have usually been developed by some analytical technique applying significant simplifications (inviscid or creeping flow and asymptotic corrections) in order to keep the problem analytically tractable [1]. Then, such models can be adopted to specific flow problems only by tayloring their forms and parameters based on measurement data.

In the last few decades, numerical experiments proved to be good alternatives to real measurements in two-phase flow modeling, just like in many other areas of physics, see e.g. [2,3,5–10,4]. However, a vast majority of studies still focus on basic problems like the study of rising bubble in a periodic box and only a few attempts have been made to get information on bubbly flows in wall bounded geometries, see e.g. [11–13].

In ligth water nuclear reactors, bubbles can appear in the fuel assemblies both in normal and accidental situations. Therefore, the accurate modeling of bubbly flows is vital both from economical and safety point of views. The fuel assemblies of ligth water reactors are usually built up as a regular array of fuel rods and the coolant flows along the rods in the so called subchannels of the assembly. Depending on the actual design, the rods are arranged in a triangular or rectangular array. The bundle is tight, which means that the cross section of the channel is narrow, usually a few square millimeters.

There are many evidences of that forces acting on bubbles in a cylindrical channel depend on the diameter ratio $\lambda = d/D$ of the bubble (d) and the channel (D) as it exceeds 0.06 and 0.12 for low and large Reynolds numbers, respectively [1]. Since the equivalent diameter of a subchannel of a rod bundle is $O(1)$ [mm], therefore wall effects can be expected to be relevant in a subchannel when the bubble diameter is $O(0.1)$ [mm] or larger.

This fact motivated us to perform numerical simulations of bubble motion in a subchannel of a rod bundle and extract information on the hydrodynamic forces acting on the bubbles from the simulation results. A lattice Boltzmann model was developed to simulate the motion of an individual bubble in the subchannel of triangular array of rods resolving the interface of the bubble. Although we have recently used a similar method for the single phase direct numerical and large eddy simulation of turbulent flows in a subchannel [17,18], here, as a first attempt, we shall limit our discussions on laminar flows. In particular, the drag and virtual mass forces are deduced from the simulation results. In our simulations, both the Eotvos and Reynolds numbers are small so the bubble remains spherical. It is demonstrated that the simulations show a consistent picture about the dynamics of bubbles in the subchannel.

* Corresponding author.
E-mail addresses: gah@aeki.kfki.hu (G. Hazi), mayer@aeki.kfki.hu (G. Mayer), amarkus@aeki.kfki.hu (A. Markus).

0017-9310/$ - see front matter © 2008 Elsevier Ltd. All rights reserved.
doi:10.1016/j.ijheatmasstransfer.2008.09.005

In Sections 2 and 3 the numerical method and the simulation results are presented, respectively. Our conclusions are given in Section 4.

2. The lattice Boltzmann method

The lattice Boltzmann method (LBM) is an innovative technique for modeling two-phase flows. Many different models have been developed in the framework of LBM to model bubbly flows see e.g. [2,14–16,5]. In this work the multicomponent–multiphase model of Shan and Chen was adopted [19]. This model has been applied for bubble flow simulations by many authors including the work of Sankaranarayanan et al. [2,3] who simulated bubble dynamics in a periodic box and extracted the drag, virtual mass and lift forces from the simulation results. Since in our problem the domain is wall bounded, there are some small differences between our approach and that of used in [2], nevertheless, for completeness, we briefly review the method we used in our calculations.

To model multicomponent flows, Shan and Chen proposed [19] to solve the lattice Boltzmann equation with Bhatnagar–Gross–Krook collision operator [20]

$$f_i^\sigma(x + c_i\triangle t, t + \triangle t) - f_i^\sigma(x,t) = -\frac{1}{\tau^\sigma}(f_i^\sigma - g_i^\sigma), \tag{1}$$

where $f_i(\mathbf{x},t)$ is the one-particle velocity distribution function, $\mathbf{c}_i$ is the lattice velocity vector, τ^σ is the relaxation time which controls the rate of approach to the local equilibrium $g_i(\mathbf{x},t)$, Δt is the time-step and $\sigma = \{1,2\}$ is for the two components, respectively.

The local equilibrium distribution is written as

$$g_i^\sigma = w_i\rho^\sigma\left[1 + 3c_{i\alpha}u_\alpha^{\sigma,eq} - \frac{3}{2}u_\alpha^{\sigma,eq}u_\alpha^{\sigma,eq} + \frac{9}{2}c_{i\alpha}c_{i\beta}u_\alpha^{\sigma,eq}u_\beta^{\sigma,eq}\right], \tag{2}$$

which is a low Mach number expansion of the Maxwell–Boltzmann distribution.

For the calculations presented in this paper we used a D3Q19 model, for which the lattice velocity vectors $\mathbf{c}_i$ and weights w_i are defined by

$$c_i = \begin{cases} (0,0,0) & i = 0 \\ (\pm1,0,0),(0,\pm1,0),(0,0,\pm1) & i = 1\ldots6 \\ (\pm1,\pm1,0),(\pm1,0,\pm1),(0,\pm1,\pm1) & i = 7\ldots18 \end{cases}$$
$$w_i = \begin{cases} 1/3 & i = 0 \\ 1/18 & i = 1\ldots6 \\ 1/36 & i = 7\ldots18 \end{cases} \tag{3}$$

The density and hydrodynamic velocity of the individual components are defined by

$$\rho^\sigma = \sum_i f_i^\sigma, \quad u_\alpha^\sigma\rho^\sigma = \sum_i c_{i\alpha}f_i^\sigma. \tag{4}$$

The velocity used in the equilibrium distribution function (2) is calculated from

$$u_\alpha^{\sigma,eq} = u'_\alpha + \frac{\tau}{\rho^\sigma}F_\alpha^\sigma, \tag{5}$$

where

$$u'_\alpha = \frac{\sum_\sigma \rho^\sigma/\tau^{\sigma\sigma}u_\alpha}{\sum_\sigma \rho^\sigma/\tau^\sigma}, \tag{6}$$

and the force F_α^σ will be defined later on.

Since we represent two-phases of a single component fluid by two components, we also define the macroscopic quantities of the mixture as

$$\rho = \sum_\sigma \rho^\sigma, \quad \rho u_\alpha = \sum_\sigma \rho^\sigma u_\alpha^\sigma + \frac{1}{2}\Delta t F_\alpha, \tag{7}$$

where

$$F_\alpha = \sum_\sigma F_\alpha^\sigma. \tag{8}$$

It can be shown that the mesoscopic evolution of the particle distribution functions (1), yields the macroscopic equations [21]

$$\partial_t u_\alpha + u_\beta\partial_\beta u_\alpha + \frac{1}{\rho}\left[\partial_\alpha(\rho c_s^2) - \sum_\sigma F_\alpha^\sigma\right] = \nu\partial_\beta^2 u_\alpha, \tag{9}$$

with some error terms, which can be neglected at low Mach numbers or can be partially compensated at higher velocities [22].

That is we solve the Navier–Stokes equations in which the viscosity is given by

$$\nu = c_s^2\sum_\sigma x^\sigma\left(\tau^\sigma - \frac{1}{2}\right), \tag{10}$$

where $x^\sigma$is the mass fraction of the component σ.

In order to model non-ideal gases, surface tension, etc. we need to choose a proper form for F_α^σ. Shan and Chen proposed to calculate the force as the gradient of particle interaction potentials ψ [19]. In this work the same methodology was used, but a new form of the interaction potential was implemented:

$$\psi^{(1)} = \frac{\rho^{(1)}}{T + C_1\rho^{(1)}} \tag{11}$$

because it can be shown analytically, that using this potential Maxwell equal area construction can be satisfied in case of a flat interface [23]. In (11) the parameter T plays the role of temperature. The coexistence curve and the measurement data of the surface tension for this potential function can be found in [25].

For the second component the potential is chosen to be simply the density, i.e. $\psi^{(2)} = \rho^{(2)}$, so the second component is an ideal gas.

Finally the interaction force is calculated as the gradient of the pseudopotential, which in the lattice Boltzmann framework can be approximated as

$$F_\alpha^\sigma = -\psi^\sigma(x)\sum_{\bar\sigma}G_{\sigma\bar\sigma}\sum_i w_i\psi^{\bar\sigma}(x + c_i)c_i, \tag{12}$$

where $G_{\sigma\bar\sigma}$ is a Green function and it controls the strength of the interactions between the components σ and $\bar\sigma$.

For the computations presented in this work our single phase lattice Boltzmann code used for turbulent rod bundle flow simulations was extended for two-components. Just like for single phase flow, the rod bundle is modeled by periodically coupling the subchannels to each other both in the lateral and axial directions. The pitch to diameter ratio of a subchannel is $P/D = 1.34$ (see Figs. 1 and 2) which value corresponds to the parameters of a fuel assembly of a VVER 440 nuclear power plant. To make the calculations fast, domain decomposition was applied in the axial directions and the computations were run in a Linux PC cluster. Walls were modeled by the interpolated bounce–back method of Yu et al. [24]. We use lattice dimensions (lattice spacing and timestep) for all dimensional quantities throughout the paper. The parameters of the interparticle potential were chosen to be $T = 13$ and $C_1 = 0.01$. The critical temperature for this model is given by $T \approx 14.6$ (see [25] for the coexistence curve and other details). The parameters, which control the interactions between the components were $G_{12} = G_{21} = 0.01$. The relaxation parameters of the components τ^σ were unity for both components.

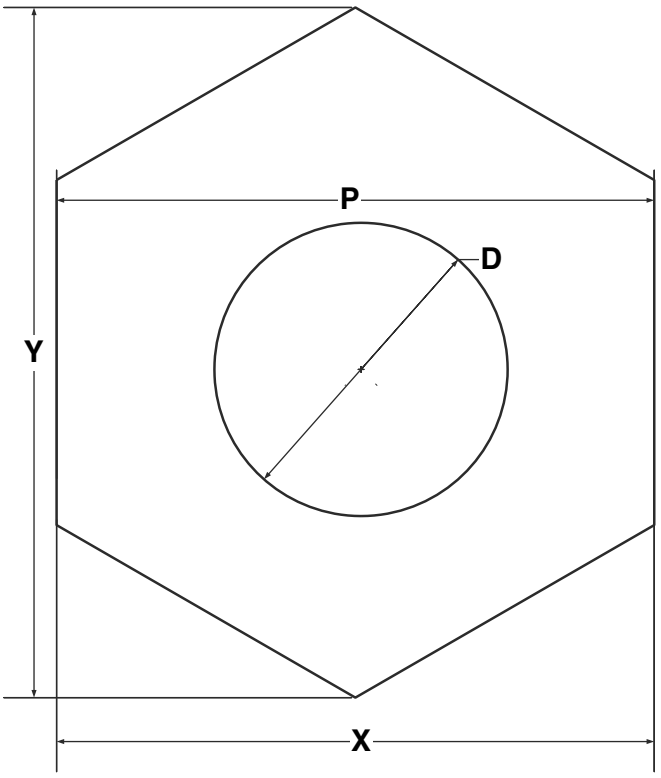

Fig. 1. Geometrical parameters of a subchannel.

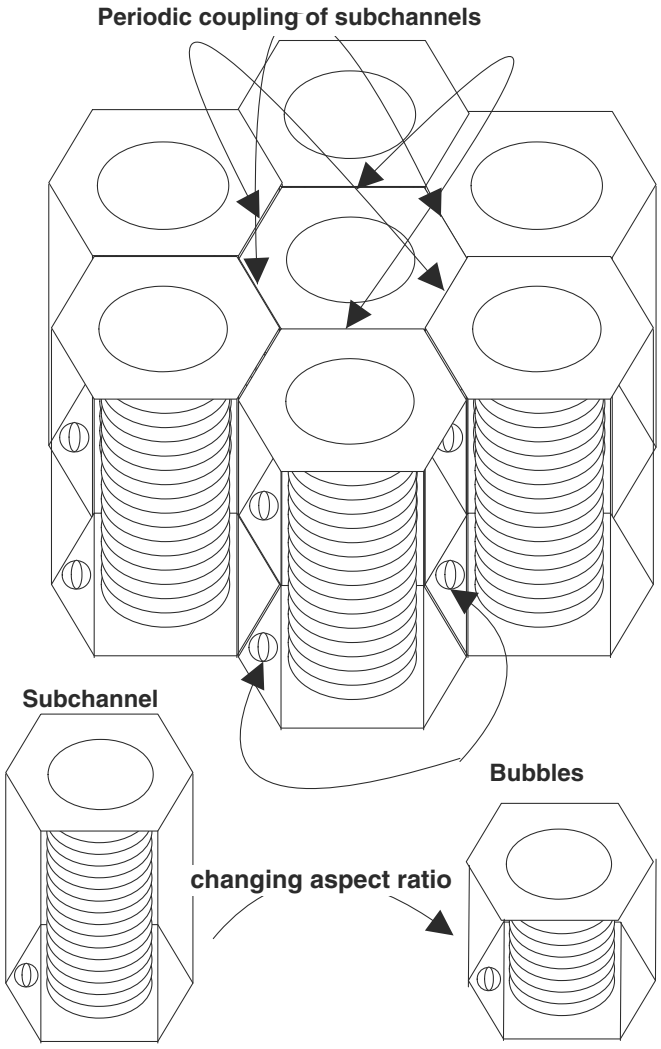

Fig. 2. Coupling of subchannels to form a rod bundle.

3. Simulation results

Using the lattice Boltzmann method, simulations have been performed introducing an individual bubble into the subchannel. The bubble was generated independently from the rod bundle simulations but using the same model parameters in a cubic box $(30 \times 30 \times 30)$ periodic in each side. The diameter of the bubble generated in this way was $d = 20$ lattice units.

Then the distribution functions obtained in the periodic box were placed at the bottom of the subchannel at a given position, as it is shown in Fig. 2. Zero velocity was initiated in the overall subchannel. Simulations started accelerating the bubble by buoyancy $F_g = g\Delta\rho$. Three different values of g were considered in the calculations $(1.5 \cdot 10^{-3}, 7.5 \cdot 10^{-4}, 10^{-4})$. For the smallest acceleration $g = 10^{-4}$ the Eotvos and Morton numbers are

$$Eo = \frac{g\Delta\rho d_{\mathrm{bub}}^2}{\sigma} = 0.3, \quad Mo = \frac{g\mu^4\Delta\rho}{\rho^2\sigma^3} = 10^{-4},$$

where σ is the surface tension and $\mu = \rho v$ is the dynamic viscosity.

Due to the periodic boundaries, the bubble interacts with itself both in lateral and axial directions. In order to obtain information on the dynamics of a single bubble in the rod bundle, three sets of simulations (Set 1–3) were performed for each g by changing the aspect ratio of the simulation domain in each set. Each set includes four runs and each run in the same set had the same aspect ratio but the domain size was varied. Since the body force was kept constant in a set, the variation of the domain cannot be considered as a higher resolution of the same domain with another size of bubble. For simplicity, details of the geometrical parameters are given in Table 1 for each simulation set.

Varying the size of the domain we could systematically study the interactions between bubbles and we could obtain information on the void fraction $\alpha = V_b/V$ dependence of the forces acting on the bubble. Here V_b is the volume of the bubble and V is the volume of the subchannel. The simulation results were then extrapolated to $\alpha \to 0$, in order to obtain information on the behavior of an isolated bubble.

Table 1
Size of bounding boxes for each simulation set

Run	X	Y	Z
Set 1			
1	142	164	108
2	156	180	120
3	194	224	150
4	208	240	160
Set 2			
1	142	164	216
2	156	180	240
3	194	224	300
4	208	240	320
Set 3			
1	142	164	324
2	156	180	360
3	194	224	450
4	208	240	480

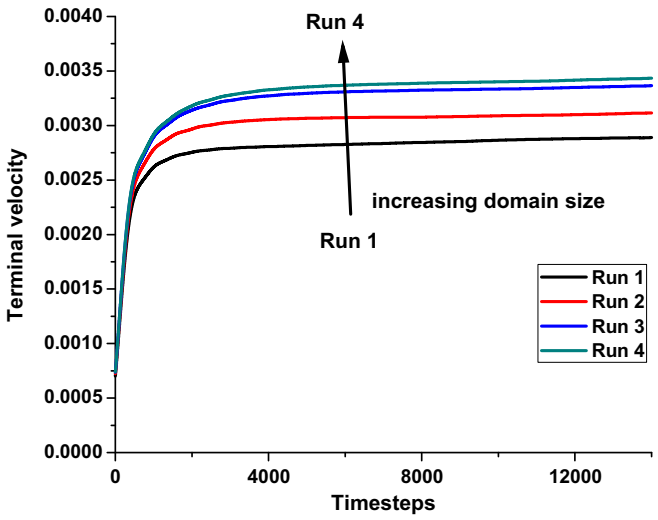

Fig. 3. Bubble rise velocity as a function of time ($g = 0.0001$, Set 2).

3.1. Bubble rise velocity

In each simulation the bubble velocity was recorded. Fig. 3 shows the evolution of the bubble velocity as a function of time in case of $g = 10^{-4}$ and for Set 2. As it can be seen, the bubble rise velocity increases rapidly at the beginning of the simulation due to the acceleration. The bubble reaches its terminal velocity, when the acceleration is balanced by the resistance of the fluid, that is by the steady drag force. Note that the terminal velocity increases as the domain size is increased. This is due to the fact that the axial and lateral interactions between bubbles (actually, the interaction of the bubble with itself) decrease as the domain size is increased.

In order to separate the lateral and axial interactions we show the terminal velocities of the second run in case of $g = 10^{-4}$ for each set (Fig. 4). That is we compare runs performed with the same lateral, but different axial sizes and consequently, only the lateral interaction changes in these runs.

As we can see the terminal velocity decreases with increasing domain length, i.e. when the axial separation of bubbles increases. Obviously, the axial interaction between bubbles is cooperative. On the other hand, we can also draw the conclusion that the lateral interaction is hindering and it has a stronger effect than the axial one, since the terminal velocity increases when the domain size is increased both in lateral and axial directions (Fig. 3).

It is worth mentioning that the same conclusions can be drawn by studying other values of g (not shown here).

In order to estimate the rise velocity of an isolated bubble, the terminal velocity of each run is shown as a function of the void fraction in Fig. 5.

In each set, the terminal velocity increases as the void fraction decreases, in line with our earlier conclusions. What is more important, the terminal velocity is in linear relation with the void fraction, so the terminal velocity of an isolated bubble ($\alpha \to 0$) can be estimated by extrapolation. In Fig. 5 the formulas obtained as linear fits are shown. For Set 2 and 3 the ordinates of the fits are very close to each other having the values 0.00361 and 0.00369, but for Set 1 it is slightly higher 0.00382. It also should be mentioned that the linear relation is less obvious for Set 1 than for the others.

Similar observations could be given for other accelerations. The estimated terminal velocity as a function of the acceleration for an isolated bubble is shown in Fig. 6. The error bars show the scattering of the extrapolated terminal velocity obtained from various sets. A linear relation can be observed between the terminal velocity and the acceleration. Note that at zero acceleration the terminal velocity should be zero, and this obvious requirement is closely satisfied by the fit of our simulation results.

In Sankaranarayanan et al. [2] bubbles rising in a periodic box were studied and it was found that the Richardson–Zaki correlation

$$\frac{u_T}{u_{T,\infty}} = (1-\alpha)^p \tag{13}$$

fits well to the numerical data, where p is the RZ exponent and $u_{T,\infty}$ is the terminal velocity of an isolated bubble. For completeness, we also plot $\log_{10}(u_T)$ as a function of $\log_{10}(1-\alpha)$ for $g = 0.00075$. In Fig. 7 one can see that the Richardson–Zaki correlation seems to work well in case of rod bundles, too; it was expected that the influence of wall bring some deviations from this correlation. On the other hand, we have three different exponents for three different configurations, although we used the same Eotvos and Morton numbers, which means that the exponents in our case depend on the configuration. Accordingly, further investigations are needed to find some useful relation for p.

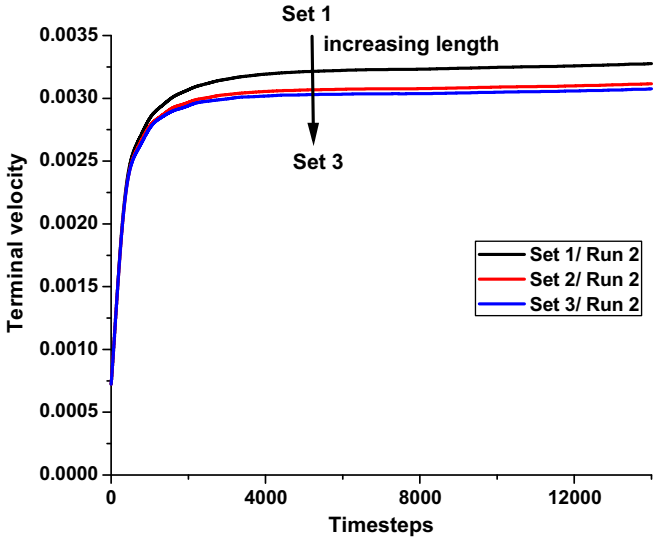

Fig. 4. Bubble rise velocity as a function of time in domains with varying length ($g = 0.0001$).

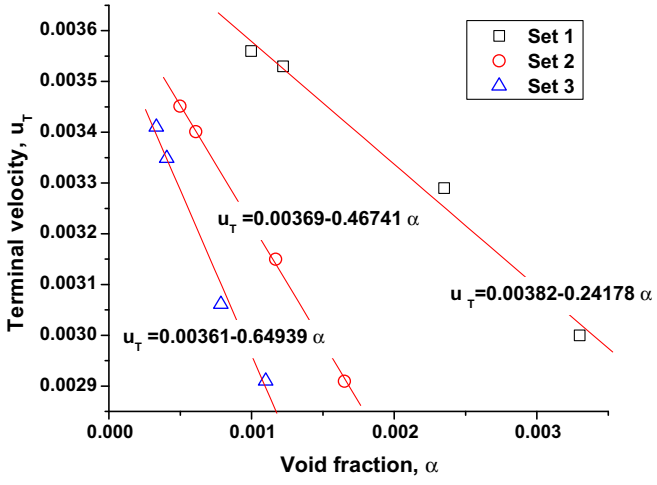

Fig. 5. Terminal velocity as a function of void fraction ($g = 0.0001$).

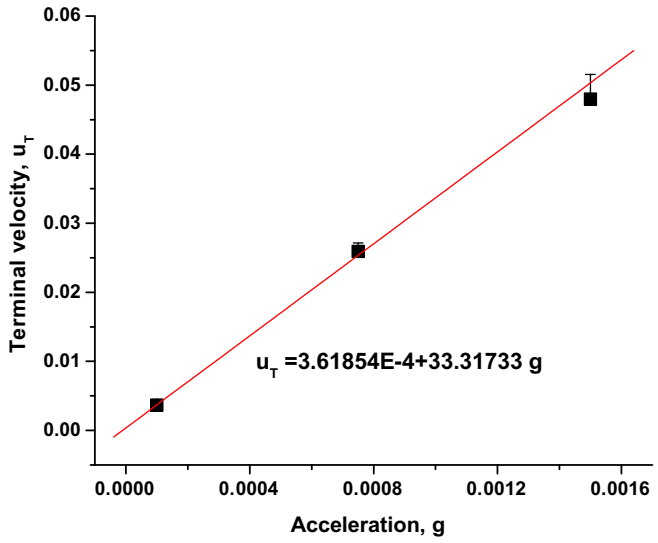

Fig. 6. Estimated terminal velocity of an isolated bubble as a function of acceleration obtained from the extrapolation of simulation data at $\alpha \to 0$.

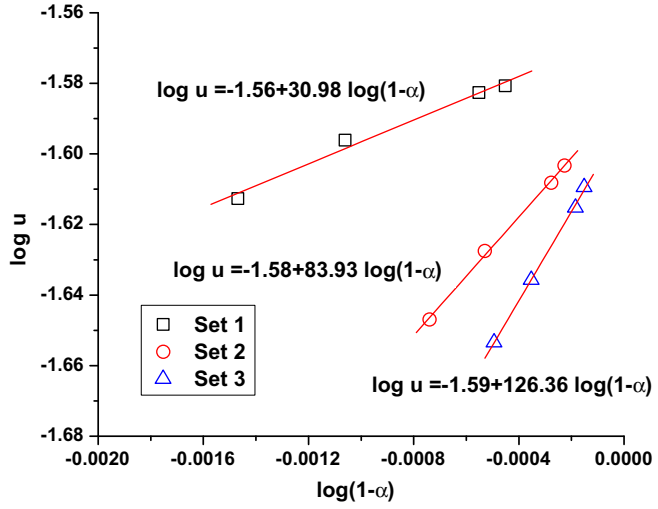

Fig. 7. Terminal velocity as a function of void fraction in a loglog plot. The slopes of the fits give the Richardson–Zaki exponent.

3.2. Drag force

As the bubble reaches its terminal velocity, the steady drag coefficient can be calculated from the force balance $F_g = F_{D,z}$, where $F_{D,z}$ is the steady axial component of the interfacial drag force, which is written as

$$F_D = \frac{1}{2} C_D A_b \rho_l u^2. \tag{14}$$

It is a well known fact that the drag coefficient C_D is a function of the bubble terminal Reynolds number [1]:

$$Re_T = \frac{u_T d}{\nu}. \tag{15}$$

In Fig. 8 the drag coefficient C_D is shown as a function of the terminal Reynolds number obtained from the simulation results and the solid line is an allometric fit for the simulation data.

As one can see, including all simulation results, we could obtain the very simple relation between the drag coefficient and the terminal Reynolds number:

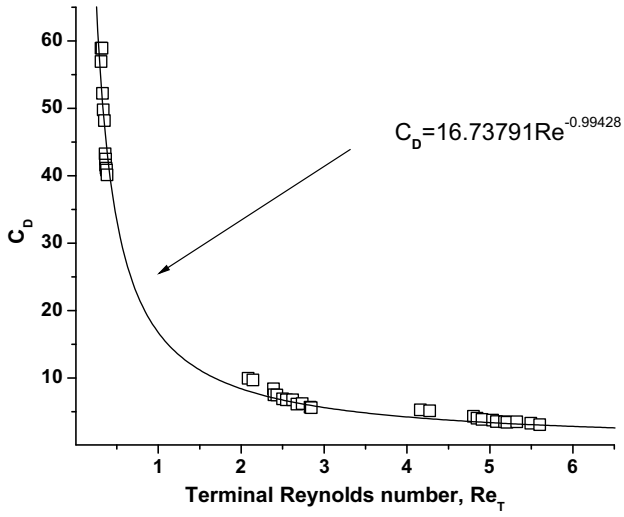

Fig. 8. Drag coefficient as a function of the terminal Reynolds number.

$$C_D \approx \frac{16.74}{Re}.$$

It is worth noting that our relation is very close to the relations:

$$C_D = \frac{16}{Re}, \quad Re \ll 1$$

$$C_D = \frac{16}{Re}\left(1 + \frac{Re}{8}\right), \quad Re \approx 1$$

$$C_D = 13.725 Re^{-0.74}, \quad 4 < Re < 100,$$

which were proposed for Stokes flow, for Stokes flow with Oseen's correction and for bubble rise at higher Reynolds numbers [1], respectively (see Fig. 9 for comparison).

Actually, the good agreement is somewhat surprising, since these relations are known to be valid in unbounded domains and in our case it was expected that wall effects increase the drag. For circulating fluid particles on the axis of cylinders, where a parabolic profile develops well upstream and downstream of the particle, a correction was proposed for the drag (see p. 232 in [1]). Since this correction is in a rather lengthy form, therefore it is not included here. However, from our point of view it is important

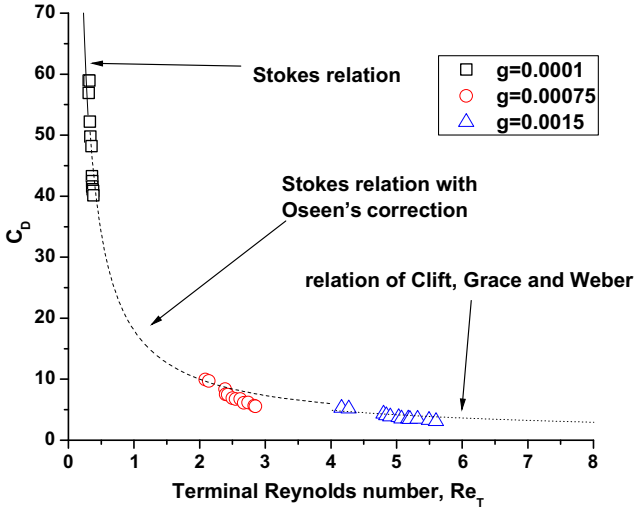

Fig. 9. Drag coefficient as a function of terminal Reynolds number and relations used in various ranges of the Reynolds number.

that the correction is strongly depends on the diameter ratio $\lambda = d/D$, where D is the diameter of the channel. In the current simulations the bubble diameter is constant, but the equivalent hydraulic diameter of the channel varies as we change the size of the domain and accordingly λ varies in the range of 0.05–0.2. In this range of parameters the wall correction factor is not significant, so the slight increase in the drag observed in our simulation data seems to be reasonable.

3.3. Virtual mass force

The virtual mass, classically found in mechanics, accounts for the acceleration of the liquid caused by the motion of the bubble. It is defined as the sum of the actual mass of the bubble and an added mass, which is due to the resistance of the surrounding fluid to acceleration. Therefore, the virtual mass can be expressed as

$$m_V = (\rho_g + C_V \rho_l) V_B, \tag{16}$$

where C_V is the virtual mass coefficient. For a single spherical bubble in an unbounded domain the virtual mass coefficient has found to be $C_V = 0.5$. If interaction between adjacent bubbles occurs the value of the virtual mass coefficient is changing. In case of wall bounded flows the virtual mass also can be a function of other parameters.

In our simulations the bubble is accelerated from rest by buoyancy. Assuming that this is the only force acting on the bubble at the beginning of the simulation, we can determine the virtual mass from the balance of buoyancy and virtual mass force:

$$g \Delta \rho V_B = m_V a, \tag{17}$$

where a is the initial acceleration of the bubble.

To determine the virtual mass coefficient we need to substitute (16) into (17), which after rearrangement can be written as

$$C_V = \frac{g \Delta \rho}{a \rho_l} - \frac{\rho_g}{\rho_l}. \tag{18}$$

To determine the initial acceleration a we calculated the time derivative of the mean gas velocity in the beginning of the simulations. It was found that the velocity is nearly linear function of time in the first few hundred steps and therefore the acceleration could be obtained as the slope of a linear fit. Then (18) was used to calculate the virtual mass coefficient. Fig. 10 summarizes the virtual mass coefficients as a function of the void fraction for $g = 0.0015$ obtained from our simulations. Just like in case of the terminal velocity, extrapolation to $\alpha \to 0$ gives the value of the virtual mass coefficient of an isolated spherical bubble in the subchannel. The extrapolations of the simulation results give consistently a value around 7.2 independently from g, which is a much higher value than usually considered for bubbles in unbounded domains ($C_V = 0.5$).

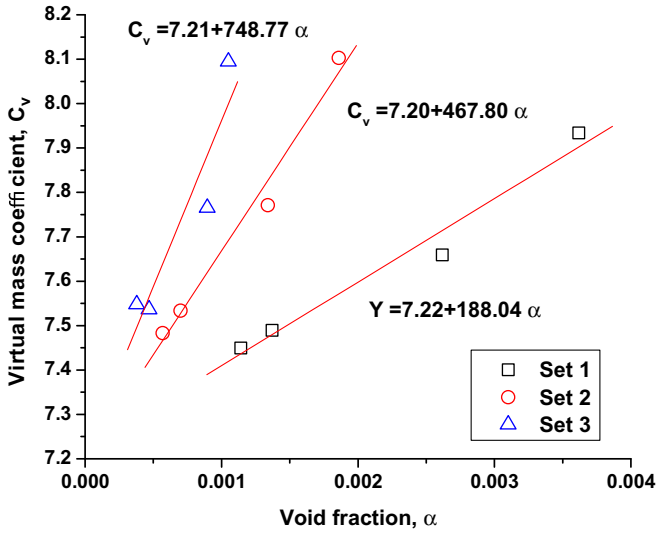

Fig. 10. Virtual mass coefficient as a function of the void fraction.

To the best of our knowledge, little is known about wall effects on the virtual mass force at low Reynolds numbers, on the other hand the increase of the virtual mass force was predicted in a number of studies using potential theory [26]. We also should keep in mind that we have assumed the only time dependent force acting on the bubble is the virtual mass force at the beginning of the simulations. However, it is well known that the modification of the base flow due to the motion of the bubble also influences on the dynamics of the bubble. Accordingly, we should take into account the entire history of the bubble motion, which is usually done by the so-called history forces. Since history force arises from the effect of diffusion of vorticity away from the surface of the bubble, it is expected that the presence of walls reduces the history force. The walls block the vorticity diffusion. When the bubble touches the walls, the diffusion is completely precluded, so the history kernel and the corresponding force decay more rapidly. Since the velocity in the liquid is very low at the beginning of the simulations, we believe that the negligence of the history force is a reasonable assumption.

4. Conclusion

Steady and unsteady drag forces acting on spherical bubbles in the subchannel of a rod bundle have been studied at low Reynolds numbers. It was found that the interactions between bubbles are similar to unbounded domains, so the axial interaction is cooperative, while the lateral interaction is hindering. The lateral interaction has been found to be stronger than the axial interaction. The interactions between bubbles change the terminal velocity of bubbles in a suspension. It was found that the Richardson–Zaki correlation can be applied in case of subchannel flows for the calculation of the terminal velocity of the suspension. However, the exponent was found to be a function of the configuration and not only that of the Eotvos and Morton numbers. Terminal velocity of an isolated bubble has been estimated by extrapolating the simulation results to zero void fraction. At the Reynolds numbers covered by the simulations $O(0.1) - O(1)$ the terminal velocity is a linear function of the gravity. The steady drag coefficient has been estimated from the force balance of buoyancy and drag forces. We observed only slight increase of the drag coefficient comparing the one obtained in this work $C_D \approx \frac{16.74}{Re}$ with well known correlations (Figs. 8 and 9). Since in our work the diameter ratio of the equivalent hydraulic diameter and bubble diameter varies in the range of 0.05–0.2, the slight increase of the drag seems to be reasonable. The virtual mass coefficient of an isolated bubble was estimated from the evolution of the bubble velocity. For an isolated bubble we obtained the value $C_V \approx 7.2$, which is a much higher value than in an unbounded domain $C_V = 0.5$. Further investigations are needed to clarify the origin of this strong deflection.

Acknowledgements

We thank Dr. Shan and Dr. Sundaresan for their help to answer questions arised in relation with the Richardson–Zaki correlation. This work has been supported by the European Integrated Project NURESIM in the 6th framework program of the European Union.

References

[1] R. Clift, J.R. Grace, M.E. Weber, Bubbles Drops and Particles, Academic Press, New York, 1978.
[2] K. Sankaranarayanan, X. Shan, I.G. Kevrekidis, S. Sundaresan, Bubble flow simulations with the lattice Boltzmann method, Chem. Eng. Sci. 54 (1999) 4817.
[3] K. Sankaranarayanan, X. Shan, I.G. Kevrekidis, S. Sundaresan, Analysis of drag and virtual mass forces in bubbly suspensions using an implicit formulation of the lattice Boltzmann method, J. Fluid Mech. 452 (2002) 61.
[4] V.K. Dhir, Numerical simulation of pool boiling heat transfer, AIChE J. 47 (2001) 813.
[5] X. Yin, D.L. Koch, R. Verberg, Lattice-Boltzmann method for simulating spherical bubbles with no tangential stress boundary conditions, Phys. Rev. E 73 (2006) 026301.
[6] E.A. Ervin, G. Tryggvason, The rise of bubbles in a vertical shear flow, ASME J. Fluid Eng. 119 (1997) 443.
[7] A. Esmaeeli, G. Tryggvason, Direct numerical simulations of bubbly flows. Part I: Low Reynolds number arrays, J. Fluid Mech. 377 (1998) 313.
[8] A. Esmaeeli, G. Tryggvason, Direct numerical simulations of bubbly flows. Part II: Moderate Reynolds number arrays, J. Fluid Mech. 385 (1999) 325.
[9] B. Bunner, G. Tryggvason, Dynamics of homogenous bubbly flows. Part 1: Rise velocity and microstructure of the bubbles, J. Fluid Mech. 466 (2002) 17.
[10] B. Bunner, G. Tryggvason, Dynamics of homogenous bubbly flows. Part 2: Fluctuations of the bubbles and the liquid, J. Fluid Mech. 466 (2002) 53.
[11] A. Esmaeeli, G. Tryggvason, A direct numerical simulation study of the buoyant rise of bubbles at $O(100)$ Reynolds number, Phys. Fluids 17 (2005) 093303.
[12] J. Lu, A. Fernandez, G. Tryggvason, The effect of bubbles on the wall drag in a turbulent channel flow, Phys. Fluids 17 (2005) 095102.
[13] J. Lu, G. Tryggvason, Numerical study of turbulent bubbly downflows in a vertical channel, Phys. Fluids 18 (2006) 103302.
[14] T. Inamuro, T. Ogata, F. Ogino, Numerical simulation of bubble flows by the lattice Boltzmann method, Future Gen. Comput. Syst. 20 (2004) 959.
[15] T. Inamuro, T. Ogata, S. Tajima, N. Konishi, A lattice Boltzmann method for incompressible two-phase flows with large density differences, J. Comput. Phys. 198 (2004) 628.
[16] I. Kurtoglu, C.L. Lin, Lattice Boltzmann study of bubble dynamics, Numer. Heat Transfer B: Fundamentals 50 (2006) 333.
[17] G. Mayer, G. Hazi, Direct numerical and large eddy simulation of longitudinal flow along triangular of rods using the lattice Boltzmann method, Math. Comput. Simul. 72 (2006) 173.
[18] G. Mayer, J. Pales, G. Hazi, Large eddy simulation of subchannels using the lattice Boltzmann method, Ann. Nucl. Energy 34 (2007) 140.
[19] X. Shan, H. Chen, Lattice Boltzmann model for simulating flows with multiple phases and components, Phys. Rev. E 47 (1993) 1815.
[20] H. Chen, S. Chen, W.H. Matthaeus, Recovery of the Navier–Stokes equations using a lattice-gas Boltzmann method, Phys. Rev. E 45 (1992) R5339.
[21] J. Chin, P.V. Coveney, Lattice Boltzmann study of spinodal decomposition in two dimensions, Phys. Rev. E 66 (2002) 016303.
[22] G. Hazi, P. Kavran, On the cubic velocity deviations in lattice Boltzmann methods, J. Phys. A: Math. Gen. 39 (2006) 3127.
[23] Hazi G. and Markus A. (2007) Consistent lattice Boltzmann methods with pseudopotential for two-phase flows, Phys. Rev. E, submitted for publication.
[24] D. Yu, R. Mei, L.S. Luo, W. Shyy, Viscous flow computations with the method of lattice Boltzmann equation, Prog. Aerosp. Sci. 39 (2003) 329.
[25] G. Hazi, A. Markus, Lattice Boltzmann simulation of boiling in subchannels, in: Proc. of The 12th International Topical Meeting on Nuclear Reactor Thermal Hydraulics (NURETH-12), Pittsburgh, Pennsylvania, USA, September 30–October 4, 2007, p. 329.
[26] X. Cai, G.B. Wallis, The added mass coefficient for rows and arrays of spheres oscillating along the axes of tubes, Phys. Fluids 5 (1993) 1614.